Molecular Structure, Computational Studies and Nonlinear Optical properties of a New Organic Chalcone Crystal

Hadjer Belahlou, Sihem Abed, Mehdi Bouchouit, Said Taboukhat, Lyamine Messaadia, El-Eulmi Bendeif, Abdelmalek Bouraiou, Bouchta Sahraoui, Karim Bouchouit

Molecular Structure, Computational Studies and Nonlinear Optical Properties of a New Organic Chalcone Crystal

Hadjer Belahlou[a,b], Sihem Abed[a], Mehdi Bouchouit[b], Said Taboukhat[c], Lyamine Messaadia[d], El-Eulmi Bendeif[e], Abdelmalek Bouraiou[b], Bouchta Sahraoui[c] and Karim Bouchouit*[a]

[a]Laboratoire de Didactique des Sciences Physiques, Chimiques et Applications, Ecole Normale Supérieure de Constantine, Ville Universitaire, Constantine, Algeria

[b]Unité de Recherche de Chimie de 1'Environnement, et Moléculaire Structurale, CHEMS, Université Frères Mentouri, Constantine 25000, Algeria

[c]University of Angers, Photonics Laboratory of Angers: LPHIA, SFR MATRIX, 2 Bd Lavoisier 49045 ANGERS cedex 2, France

[d]Laboratoire Energétique Appliquée et Matériaux (LEAM), Université de Jijel, Ouled Aissa, Jijel, Algeria

[e]CRM2 UMR, CNRS 7036, Université de Lorraine, F-54000Vandæuvre-lès-Nancy, France

Abstract

A new conjugated chalcone compound (Z)-2-(1-(1-(2,4-dimethylphenyl)-3-oxo-3-phenylprop-1-en-2-yl)pyridin-2(1*H*)ylidene) malononitrile was prepared and structurally analyzed using single-crystal X-ray diffraction. This new compound's quadratic and cubic susceptibilities at 1064 nm were analyzed and evaluated using the second and third harmonic generation methods after deposition in PMMA polymer thin films. These films have been used for the induced second harmonic generation measurements achieved using the corona poling technique. Complementary information on electric dipole moment, static dipole polarizability, and initial hyperpolarizability of this compound were obtained from the density functional theory (DFT) calculation performed at the DFT/B3LYP/6-311G++ (d, p) and Gaussian 09 software. The findings demonstrate that when compared to previous chalcone NLO crystals that have been published, the synthesized crystals had greater crystal transparency, polarizability, and π-conjugation. In particular, the (Z)-2-(1-(1-(2,4-dimethylphenyl)-3-oxo-3-phenylprop-1-en-2-yl)pyridin-2(1*H*)ylidene) malononitrile crystal's SHG and THG susceptibility are 0. 243 [pmV^{-1}] and 41.13 10^{-22} [m^2V^{-2}], respectively. The combined findings demonstrate that the NLO

properties depend only on the steric hindrance and the chemical structure, that is, the system of π-conjugated electrons.

Keywords: Chalcone, NLO, THG, SHG, X-ray diffraction, DFT.

1.Introduction

Electronic organic compounds with quadratic and cubic nonlinear optical properties have attracted significant attention for their potential application in optoelectronic devices in the last forty years. When nonlinear optical compounds interact with an electromagnetic field, they produce electromagnetic radiation with a frequency and amplitude that differs from the input. NLO active materials are of great interest due to their extensive sensing, optical limiting, photovoltaic devices, optical switching, visual communications, data storage, signal processing, etc. [1-4]. Therefore, designing new materials with high NLO response is of utmost desire for industry and academia. The nonlinearities of the electronic organic compounds can be higher by associating transition metals; this is generated by the effect of f-electrons on the nonlinearities response of lanthanide-doped coordinated complexes observed by Maury et al. [5]. Many investigations on the NLO properties of electronic organic compounds have found that the direct participation of p-electrons improves the NLO response. Similarly, the literature illustrates that organic electronic chromophores compound quadratic and cubic nonlinear responses increase upon a π-conjugated system. A vast class of materials with strong nonlinearity, strong quadratic and cubic NLO responses, and excellent optical damage threshold levels are organic nonlinear optical materials, specifically those with delocalized electrons [6-8].

The molecules centrosymmetric must behave in low-energy charge-transfer transitions and be significantly different between the excited state dipole moment and the ground state dipole moment to have a high quadratic NLO response. Electronic chromophores compound also presented promise due to their low energy observed from interatomic and intermolecular interactions charge transfer (CT) excited states. An informed choice of nature can easily control these interaction's intensity and energy, electron withdrawing and donating groups. Furthermore, their strong nonlinearities made them competitive concerning organic compounds and interest in optoelectronic applications [9-12]. The quadratic and cubic optical nonlinearities that come from the π conjugated system, which generally exist in the class of the chalcone compounds, have drawn the attention of chemists and physicists. Also, due to their significant charge transfer via the substituent groups on the aromatic rings, chalcone derivative molecules with a conjugated system exhibit a perfect NLO system. For example, compound 1, which

belongs to this family, has two aromatic rings joined by a propene unit, made of three carbons with a carbonyl group and one unsaturation. The π-conjugated system in their chemical structure creates a broad charge transfer axis with suitable electron donor and electron acceptor substituent groups on the aromatic terminal rings.

Photoactive electronics chalcone derivatives compounds are particularly appealing because of their best quadratic nonlinearities responses and because they are used in various fields of electroluminescent devices, in chloroform sensitized for photovoltaic cells, in laser technology, in image processing, as bio-imaging processing [13-21], and in light-sensitive medicine.

Our earlier research [22-29] shows the causes of nonlinear responses and the relationship between chemical structure and nonlinear features. We describe in detail the following four novel organic electronic heterocyclic chalcone derivatives' synthesis, characterization, optical, and NLO findings. In addition, the cubic and quadratic nonlinear of one conjugated chalcone characteristics were assessed.

2. Experiment

2.1. Materials and instrumentation

All the reagents and solvents were purchased from Aldrich, Acros Organics, and Merck and used without further purification. The melting point was determined using a Büchi M-565 Automatic Melting Point Apparatus. The NMR spectra of 1 was recorded on a Bruker Avance 250 MHz mixture of $CDCl_3$ and DMSO-d^6. and the FT-IR spectrum was recorded on a Thermo Scientific Nicolet iS50 FTIR spectrophotometer.

2.2. Synthesis

1 mmol of 2-chloro-1-(2-oxo-2-phenylethyl)pyridin-1-ium bromide (1) and 0.75 mmol of 2-benzylidenemalononitrile derivatives are introduced into a flask containing 5 mL of acetonitrile. 0.1mL of triethylamine was added. The solution is irradiated in an ultrasound bath at room temperature for 4 h (the progress of the reaction is monitored by TLC, chloroform was used as eluent). The reaction mixture was poured onto a cooled saturated NaCl solution. The product is extracted from the aqueous phase with ethyl acetate. After evaporation of the solvent, the solid obtained is recrystallized using acetonitrile as solvent.

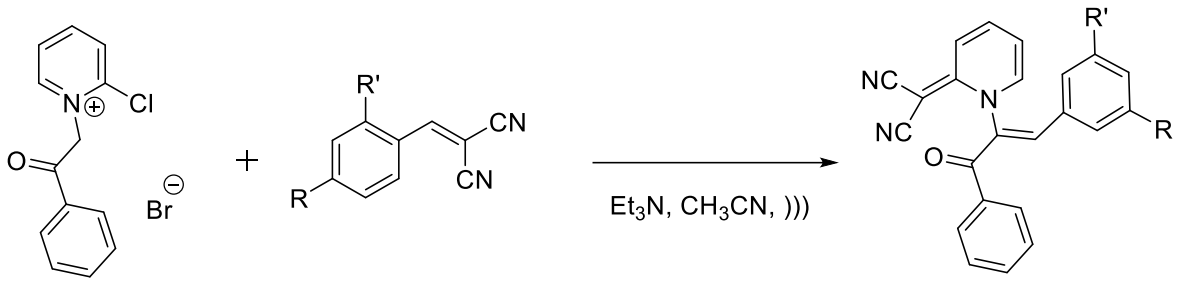

1: R'=R=Me (78%)
2:R'=R=H (72%)

Scheme 1. Synthetic scheme of studied compounds 1 and 2.

Compound **1** and **2** were synthesized as shown in scheme 1 according to our previous work [28]. **Compound 1:** Yield: 78%; mp.= 235°C; IR (cm^{-1}): 2195, 2167, 1644, 1634, 1539, 1492, 1446, 1266, 1173 ; ^{1}H NMR ($CDCl_3$, 250.13 MHz) δ (ppm): 8.09 (s, 1H), 8.02 (d, J=6.8Hz, 2H), 7.83-6.83 (m, 9H), 6.63-6.57 (m, 1H), 2.33 (s, 6H); ^{13}C NMR ($CDCl_3$, 62.9 MHz) δ (ppm): 190.0, 156.2, 143.1, 142.9, 140.6, 140.0, 137.7, 136.3, 136.1, 132.7, 132.3, 129.8, 129.5, 128.7, 128.3, 127.9, 126.5, 122.4, 119.6, 113.2, 45.2, 21.6, 20.3.

Compound 2: This compound was described previously and its structure was determined using ^{1}H NMR, IR, UV and X-ray spectroscopic methods in our previous work [28].

2.3. Single-crystal X-ray diffraction measurements

The single-crystal X-ray diffraction analysis were carried out at 100 K on a Rigaku SuperNova dual-wavelength microfocus diffractometer, equipped with a 135 mm Atlas CCD detector, using Cu-K_α radiation (λ=1.54184 Å). The CrysAlis program suite was used for data collection, reduction, and analytical absorption corrections. Direct methods and successive Fourier difference syntheses were used to solve the crystal structures, which were then refined using the weighted full-matrix least-squares method against F^2 using SHELXL [30]. Tab 1 summarizes the crystal data, data collection, and structure refinement details. Anisotropic refinement is applied to all non-hydrogen atoms. For bond length distances and riding restraints, all H atoms were located in difference Fourier electron-density maps and treated as riding on their parent atoms, with C-H = 0.950 and Uiso(H) = 1.2x Uiso(C), respectively. The WinGX software package was used to perform all calculations [31]. The studied compounds' cif-file can be found in the Cambridge Structural database under the number CCDC 2235542.

On request to the Director, CCDC, 12 Union Road, Cambridge CB2 1EZ, UK, fax: +44 (0)1223 336033, or email: deposit@ccdc.cam.ac.uk, free copies of the available material can be obtained.

Table 1. Crystal data, data collection and structure refinement for the studied compound

Compound	**1**
Chemical formula	$C_{25}H_{19}N_3O$
M	377.45
Crystal system	triclinic
space group	P -1
a (Å)	8.5595(4)
b (Å)	9.1785(5)
c (Å)	13.7814(7)
α (°)	105.584(5)
β (°)	97.794(4)
γ (°)	102.016(4)
V (Å^3)	998.76(9)
Z	2
T (K)	100
μ (mm^{-1})	0.617
Crystal size (mm)	0.19×0.09×0.3
Radiation type	Cu-K_α
Diffractometer	Rigaku SuperNova
R_{int}	0.0175
θ_{min}, θ_{max} (°)	3.400; 76.817
No. of measured reflections	11444
No. of independent reflections	4098
No. of observed [I > 2(I)] reflections	3810
No. of parameters	266
No. of constraint/restraint	0
$R[F^2 > 2\sigma(F^2)]$	0.049
$wR(F^2)$	0.137
S	1.073

2.4. Thin film preparation and optical absorption measurements

The film of the studied compound was prepared from a Dimethyl sulfoxide (DMSO) solution of PMMA matrix (Sigma-Aldrich, Mw=350,000 g mol^{-1}) and **1** with the ratio 20:5. Spin-coater (SCS G3) at 1000 rpm was used to elaborate thin films on cleaned glass substrates. To evaporate any remaining solvent, thin films were kept in the oven for 4 hours at 60° C. The prepared thin film thickness was measured with a profilometer (Dektak 6M) and found between 147 and 247 nm. The obtained values of thickness and absorption peaks are grouped in Tab. 2.

Table 2: Thickness, absorption peaks and values of absorption coefficients.

Sample	Thickness [nm]	λabs	α [10^3 cm^{-1}]	
			355 nm	532 nm
1	(247.00 ± 2.81)	322; 375	12.61	2.29
2	(145.92 ± 1.21)	391	6.78	0.31

2.5. Nonlinear optical measurements

The measurements of the second harmonic (SH) and third harmonic (TH) were done with a well-known Maker fringe setup [32, 33]. The intensity of generated harmonics as a function of incident angle was measured in s and p polarization when thin films rotate from -75° to +75°. For THG measurements, no restriction of polarization has been observed. The laser beam's fundamental wavelength was 1064 nm, frequency of 10 Hz, 30 ps pulse duration, and energy of 60 mJ.

- **SHG analysis:**

To evaluate the quadratic nonlinear optical susceptibility, we have used the Lee model [34]:

$$\chi^{(2)} = \chi^{(2)}_{Quartz}\left(\frac{2}{\pi}\right)\left(\frac{L^{coh}_{Quartz}}{d}\right)\left(\frac{\frac{\alpha d}{2}}{1-exp\left(-\frac{\alpha d}{2}\right)}\right)\sqrt{\frac{I^{2\omega}}{I^{2\omega}_{Quartz}}} \qquad (1)$$

Where: $\chi^{(2)}_{Quartz} = 1 \cdot 10^{-12} m \cdot V^{-1}$**[35]**, $L^{coh}_{Quartz} = 21\ \mu m$ is the reference material's coherence length, d: is the sample thickness, α: linear absorption coefficient, $I^{2\omega}$ and $I^{2\omega}_{Quartz}$ are the thin film and reference material's SHG intensities, respectively.

- **THG analysis:**

Cubic nonlinear optical susceptibility was calculated using the Kubodera-Kobayashi model [36]:

$$\chi^{(3)} = \chi_s^{(3)} \left(\frac{2}{\pi}\right)\left(\frac{l_{c,s}}{d}\right)\left(\frac{\frac{\alpha d}{2}}{1-e^{-\frac{\alpha d}{2}}}\right) \quad (2)$$

Where; $\chi_{Silica}^{(3)} = 2 \times 10^{-22} m^2 \cdot V^{-2}$ [37], $L_{Silica}^{coh} = 6.7\mu m$ is the reference material's coherence length, d is the sample thickness, an $I^{3\omega}$and $I_{Silica}^{3\omega}$ are the thin film and reference material's THG intensities, respectively.

The theoretical model utilized accounts for optical absorption at the third harmonic wavelength, but it is no longer applicable when non-linear absorption is present as a function of laser intensity.

Generally, second harmonic generation depends on the symmetry of the medium, it is known that is impossible to obtain SHG response in centrosymmetric structure. In the case of the guest-host system, SHG is possible by creating macroscopic non-centrosymmetry. This is achieved, using the corona poling method [38]. In the first stage, a thin film is heated to a temperature close to the glass transition temperature of polymer (in the case of PMMA about 105°C) and the temperature is hold constant. High voltage is then applied (typically a few kilovolts, in our case 6 kV) for a certain amount of time (about 60 minutes in our case) and then the sample is cooled to room temperature while maintaining the high voltage. In this technique during polymer heating, the molecules can "move" and the dipole moments orient themselves in the direction of the applied electric field. After reaching RT, the high voltage is switched off and the dipole moments remain frozen for a long time

2.6. Computational details

Quantum chemical calculations were carried out using the Gaussian 09 program, and Gauss View was used for visualization [39,40]. The molecular structures of molecules **1** and 2 were optimized for the ground state by the density functional theory (DFT) method combined with B3LYP hybrid functional at 6-311G (d, p) basis set in the gas phase [41,42]. Stationary points have been positively identified for global minima without imaginary frequencies. All the quantum chemical parameters, such as E_{HOMO}, E_{LUMO}, energy gap, dipole moment (μ), average polarizability, anisotropy of the polarizability, first static hyperpolarizability and second hyperpolarizability were calculated and discussed. Time-Dependent Density Functional Theory (TD-DFT) was used to calculate electronic excitation energies for molecules.

- **NLO response of the title compounds**

The NLO properties, such as first static hyperpolarizability (β_0) , second hyperpolarizability and the related properties (α, β and $\Delta\alpha$) of the studied compounds, were calculated using DFT theory at B3LYP/6-31+(d) basis set, based on the finite field approach. The First hyperpolarizability is a third-rank tensor that a 3 x 3 x 3 matrix can describe. The 27components of the 3D matrix can be reduced to 10 due to the Kleinman symmetry [43]. The total dipole moment µ, the average polarizability α, anisotropy of the polarizability $(\Delta\alpha)$, first static hyperpolarizability (β_0), and average second hyperpolarizability (γ) frequency depended (0.043 a.u.) were computed using the following relations, and the results are given in Table 7.

$$\mu = (\mu_x^2 + \mu_y^2 + \mu_z^2)^2$$

$$\langle\alpha\rangle = \frac{\propto_x + \propto_x + \propto_x}{3}$$

$$\Delta\alpha = \frac{1}{\sqrt{2}}[(\propto_{xx} - \propto_{yy})^2 + (\propto_{yy} - \propto_{zz})^2 + (\propto_{zz} - \propto_{xx})^2 + 6\propto_{xx}{}^2]^{1/2}$$

$$\beta_0 = (\beta_x^2 + \beta_y^2 + \beta_z^2)^{1/2} \quad \text{and} \quad \beta_x = \beta_{xxx} + \beta_{xyy} + \beta_{xzz}$$

$$\beta_y = \beta_{yyy} + \beta_{yzz} + \beta_{yxx}$$

$$\beta_z = \beta_{zzz} + \beta_{zxx} + \beta_{zyy}$$

$$\gamma = \frac{1}{5}(\gamma_{xxxx} + \gamma_{yyyy} + \gamma_{zzzz} + 2\gamma_{xxyy} + 2\gamma_{xxzz} + 2\gamma_{yyzz})$$

The (β) components of GAUSSIAN 09 output are reported in atomic units and therefore the calculated values are converted into e.s.u. units (1a.u = 8.6393×10^{-33}e.s.u). On the other hand, the reactivity parameters of two compounds were also calculated to elucidate the reactivity of the molecules with the energies of LUMO and HOMO using the following relations:

$$\boldsymbol{\chi = -\mu = \frac{(E_{HOMO} + E_{LUMO})}{2}} \qquad (3)$$

$$\boldsymbol{I = -E_{HOMO}} \qquad (4)$$

$$\boldsymbol{A = -E_{LUMO}} \qquad (5)$$

$$\boldsymbol{\eta = \frac{I - A}{2} = -\frac{(E_{HOMO} - E_{LUMO})}{2}} \qquad (6)$$

$$\sigma = \frac{1}{\eta} \qquad (7)$$

$$\omega = \frac{\mu^2}{2\eta} \qquad (8)$$

I and A represent the ionization potential and electron affinity, respectively. These quantities are associated with and with Koopman's theorem [44].While χ, η and σ signify the electronegativity, hardness and softness of molecule, respectively. The molecule has high hardness (hard), high softness (soft) values and a large frontier orbital gap, which means that the molecule is associated with low chemical reactivity and high kinetic stability. In comparison, the low softness values mean that the molecule easily changes the electron density with its environment. The high value of electrophilicity (ω) and chemical potential (μ) indicate the ability of the molecule to accept electrons [45-47].

3. Results and discussion

3.1. Synthesis

Compound **1** and **2** represented in scheme **2** were synthesized according to our previous work [28] from 1 mmol of 2-chloro-1-(2-oxo-2-phenylethyl)pyridin-1-ium bromide salt and 2-benzylidenemalononitrile derivatives in the presence of triethylamine as catalyst. The reaction was conducted in an ultrasound bath at room temperature.

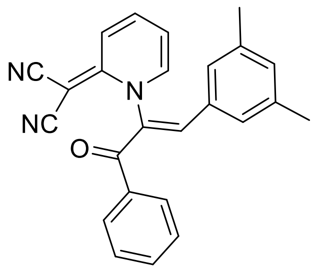

1

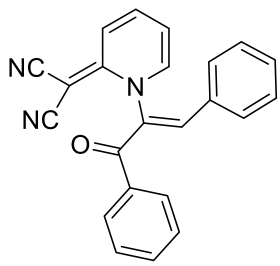

2

Scheme 2. Formula of studied compounds **1** and **2**.

The structure of compound 1 has been confirmed by IR, ^{1}H and ^{13}C NMR spectroscopy. The IR spectrum of compound 1 showed the presence of two C≡N groups by two bands at 2167 and 2195 cm^{-1}, and showed one sharp band at 1634 cm^{-1} due to vibration of the carbonyl (C=O) group. The ^{1}H NMR spectrum of compound 1 indicated a singulet at 2.33 ppm corresponding to the two methyl protons. The aryl proton signals appeared between 8.09 and 6.57 ppm (12H,

m). The ^{13}C NMR of compound 1 showed a signal at 190.0 ppm, attributed to the carbonyl carbons. The other carbones appeared between 156.2 and 113.2 ppm.

3.2. Structural commentary

Single crystals of compound **1** were grown by crystallizing the crude products in hot acetonitrile as solvent. According to a single crystal x-ray diffraction analysis on a yellow-colored crystal, the molecular structure of this chalcone ((E)-2-(1-(1-(2,4-dimethylphenyl)-3-oxo-3-phenylprop-1-en-2-yl)pyridin-2(1H)ylidene) malononitrile) crystallizes in the triclinic crystal system and belongs to the P-1 space group. The asymmetric unit of **1** is shown in Figure 1.

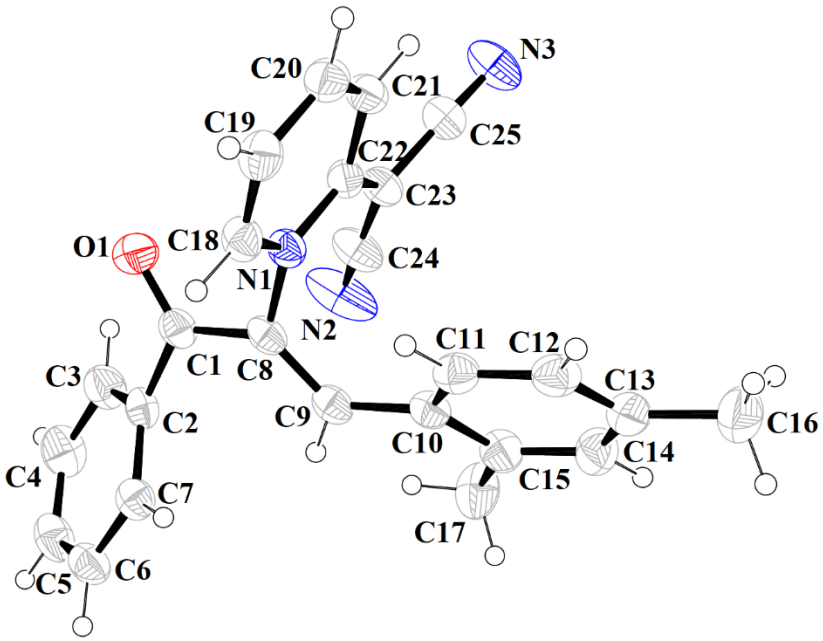

Figure.1. The molecular structure of **1** showing the atom numbering scheme.

This compound has aromatic rings, only one of which is disubstituted by two methyl groups. Due to the E geometry of the chalcone alkene, the two phenyl rings are tilted towards the same side of the molecule. The structure of the molecule is highly conjugated in two crossed planes. The examination of three torsion angles confirmed the nonplanarity of this molecule. The angles involving the aromatic rings are equivalent, with a small bend. where the link C3—C2 and C1—C8 has a torsion of -142.14° and the bonds C15—C10 and C9—C8 have a torsion of -145.11(15)°. Despite a planarity breach, the chalcone's torsion angle between the C9—C8 and C1—O1 links is -164.23(14)°.

The phenyl ring is nearly wholly planar, but the benzoyl group exhibits a non-planar structure, and we see that the O1 atom has been significantly displaced (by 0.863(2) Å) from the average ring plan. The C9–C10, C1–C8, and C1–C2 bond lengths of 1.462(1) Å, 1.490(1) Å, and

1.488(1) Å, respectively, in the propene bridge, clearly indicate the bond type of this segment. While the lengths of the C8-C9 and C1-O1 bonds, 1.222(1) Å and 1.343(1) Å, respectively, indicate the nature of these bonds. The values 131.64(9)° and 119.91(8)° coresponding to the bond angles of the C8—C9—C10 and C2—C1—C8, respectively, indicate the sp^2 hybridization of the C1, C8, and C9 carbon atoms. The examined compound's three-dimensional crystal packing comprises weak C—H...N and C-H...O hydrogen bonds connecting organic molecular species. Weak C-H-C and C-H...O intermolecular interactions are another characteristics of the three-dimensional network. Remarkably, the malononitrile N3 exhibits a distinct behavior. However, it only takes part in one C—H...N hydrogen bond. Therefore, the network of intermolecular interactions does not also include the N3. It is noteworthy that the pyridine ring and the benzoyl group are stacked similarly. To produce this configuration, the carbonyl group and a nearby benzoyl group interact via C-H...O interactions. One observes that compound 1 intermolecular contacts network is more advantageous for effective charge transfer.

Table 3: Distances (Å) and angles (deg) for hydrogen bonds in compound 1

D–H…A	*d*(D–H)	*d*(H…A)	*d*(D–A)	D–H–A	Symmetry
Compound 1					
C21—H21···O1^{i}	0.95	2.45	3.2731 (18)	145	-x,1-y,1/2+z
C18—H18···N3^{ii}	0.95	2.48	3.331 (2)	149	1/2+x,1/2-y,z

Symmetry codes: (i) *-x*, *-y*+1, *-z*; (ii) *x*+1, *y*, *z*.

The slipperiest π – π stacking, with a centroid-centroid distance of 3.6581(6) Å between the phenyl rings and C-H interactions, solidify the packing (Table 4). As seen in the current example, interactions, while significantly weaker than coordinative bonds, are crucial for forming multidimensional networks in the solid state.

Table 4: Intermolecular and intramolecular interactions **C-H…Cg** (C–H… π, Å,°) operating in the crystal structure of 1.

D–H…A	*d*(C–H)	*d*(H…Cg)	*d*(C–Cg)	C–H–Cg	Symmetry
Compound 1					
C11—H11···Cg1	0.95	2.82	3.4191(11)	124	X,Y,Z
C17—H17a···Cg2	0.95	2.86	3.8068(13)	170	2-X,2-Y,1-Z
C19—H19···Cg2	0.95	2.96	3.7918(12)	149	2-X,1-Y,-Z

Cg1 (C1 C2 C3 C4 C5 C6 C7), Cg2 (C10 C11 C12 C13 C14 C15).

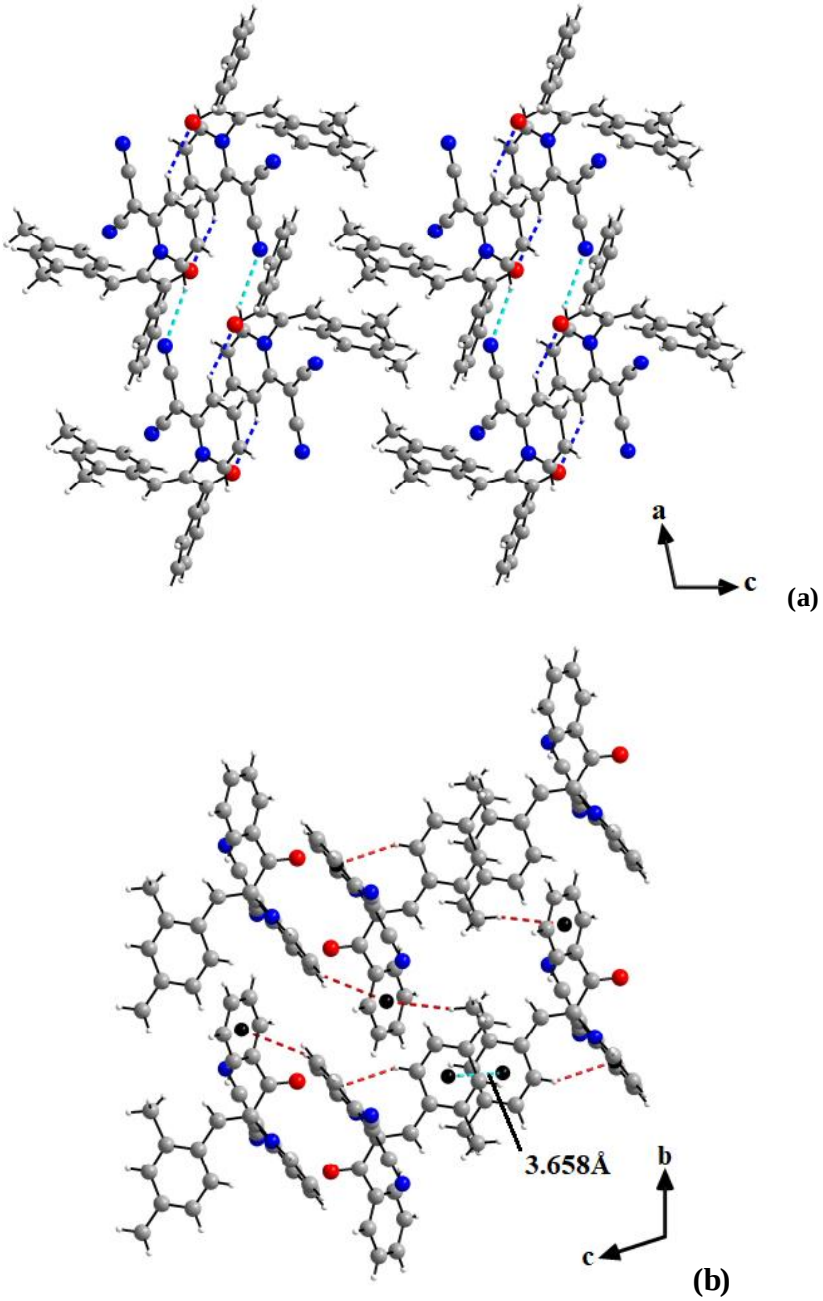

Figure 2. (a) Projection along the a axis of the atomic arrangement of I. Dotted lines represent the hydrogen bond. (b) Alternating layers parallel to (010) plane of 1 at b = 1/2, viewed via a axis. Intermolecular and intramolecular interactions C–H… π are shown as red dashed lines.

3.3. Hirshfield surface analysis

Analysis and calculations of the Hirshfeld surface [48] were carried out with CrystalExplorer17.5 [49]. We may investigate hydrogen bonding interactions using a Hirshfeld surface, which is built using normalized distances (d_{norm}) [50,51]. On the surface, red areas represent smaller interatomic interactions while blue areas represent greater interatomic contacts. The area of a Hirshfeld surface that is white denotes connections where the distance

between the linked atoms is equal to the total of their van der Waal radii.

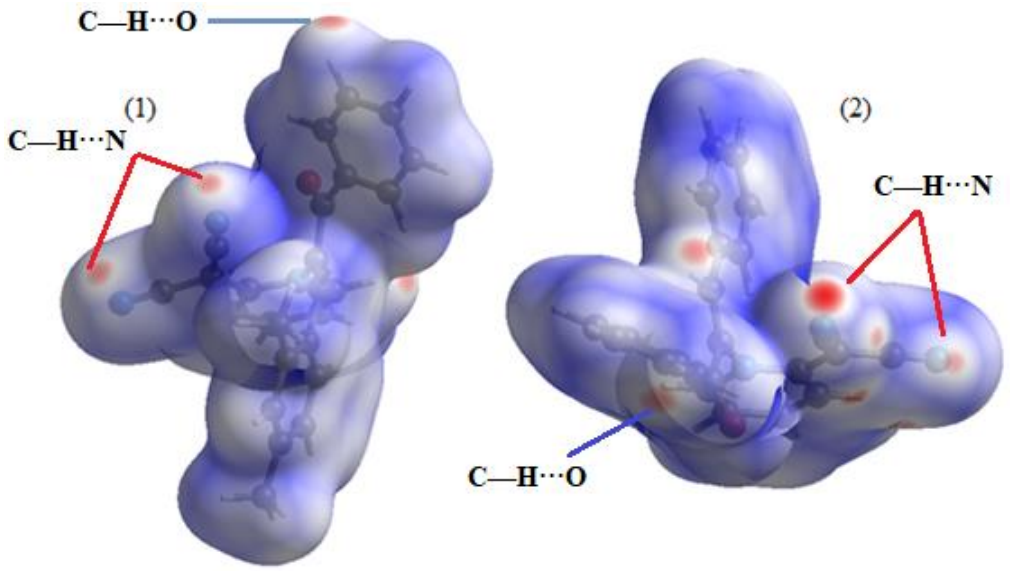

Figure 3a. View of the three-dimensional Hirshfeld surface of the studied compounds **1-2** plotted over dnorm.

The dnorm plots in the studied compounds were mapped with a color scale between -0,3099 a.u. (blue) and 1.4598 a.u. (red) for compound 1 and -0,2429 a.u. to 1.1203 a.u. for **2** are shown in Fig. 3a. In both compounds the red spots indicate the contribution of C—H···O and C—H···N hydrogen bonds. The plots for whole interactions are represented in Figure 3a.1 for compound **1** and 3a.2 for **2**. The largest spikes on these plots stand for H···H contact. A small difference is found in the interatomic contacts of **1** and **2**. For **1**, the contact of utmost importance is H···H (45%, Figure 3c), whereas, for 2, the contact of utmost importance is O···H (37.1%).

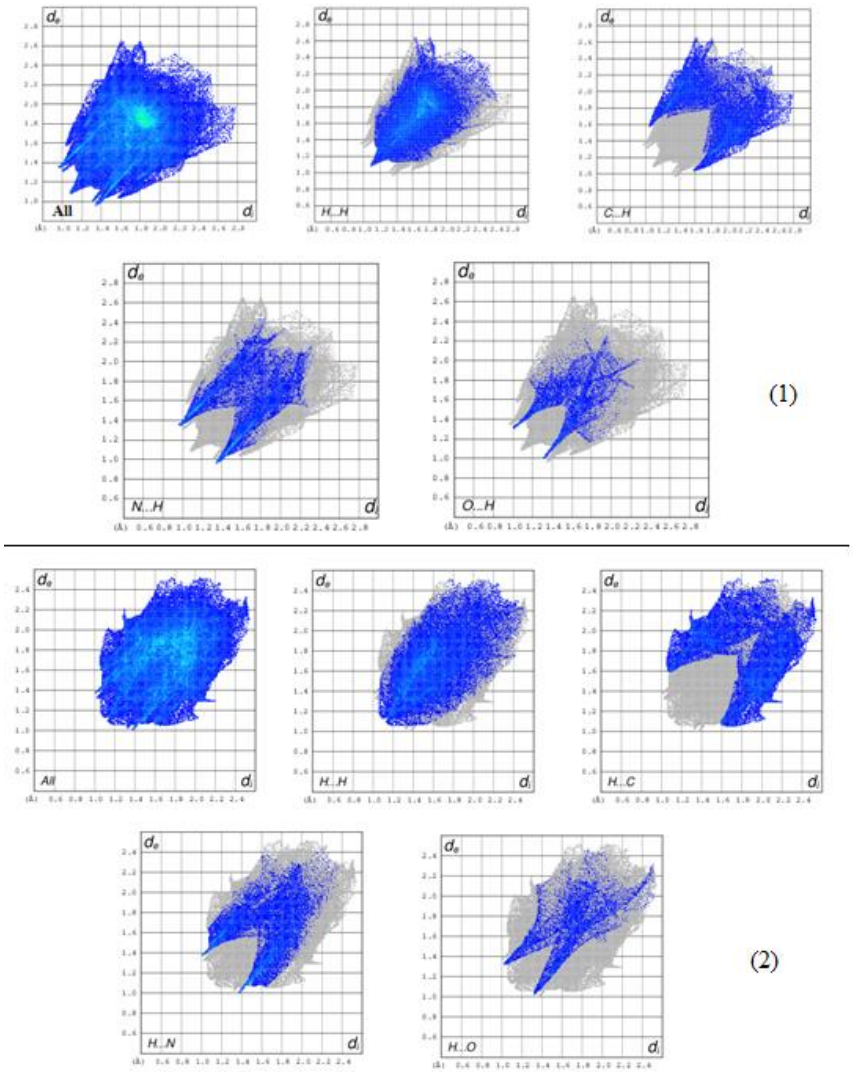

Figure 3b. 2D fingerprint plots of compound 1-2 (a) shows reciprocal contacts resolved into O…H, N…H, C…H, and H…H. Part figure shows percentage contact contributions to the total Hirshfeld surface area of the molecule. Black arrows show the spike for different interactions; d_i is the closest internal distance from a given point on the Hirshfeld surface, and d_e is the closest contact point external to the surface of the molecules.

Figures 3b-c shows the extended two-dimensional fingerprint plots [52], where de and di are the relative distances from the Hirshfeld surface to the closest nuclei on the outside and inside of the surface. H...H contacts account for 44.7% of the crystal packing, followed by C...H/H...C contacts (25.1%), N...H/H...N contacts (16.3%), and O...H/H...O contacts (6.9%) for compound **1** and for **2** as a result : H...H contacts account for 37.1%, followed by C...H/H...C contacts

(27.4%), N...H/H...N contacts (17.7%), and O...H/H...O contacts (7.8%).

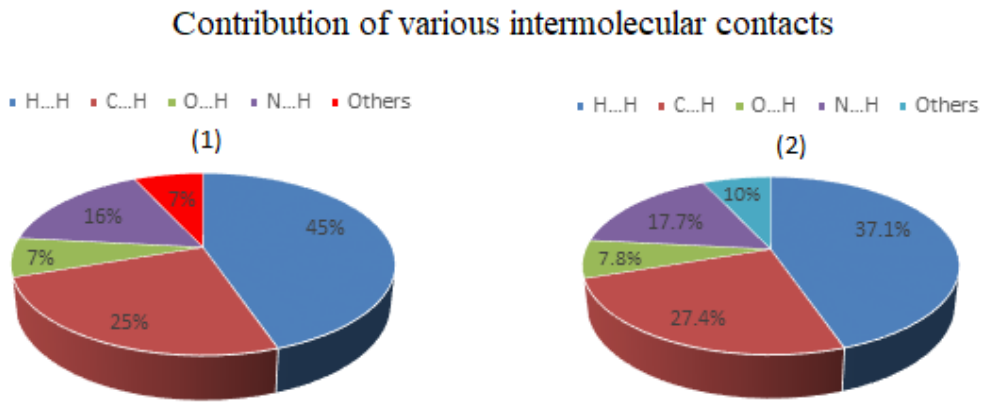

Figure 3c. Relative contribution of various intermolecular interactions to the Hirshfeld surface area in the studied compounds **1-2**.

These results show that both compounds' interatomic and intermolecular interactions occur similarly. So we can conclude that all these contacts do not affect the nonlinear optical properties response and depend only on the steric hindrance and the chemical structure (the system of π-conjugated electrons).

3.4. UV-visible spectra

Figure 4 shows the absorption spectra thin film of the studied compound. The absorption band maxima are observed at 300 and 390 nm, respectively, assigned to the π→π * and n→π* transitions. We can also see that the studied chalcone has high transparency at wavelengths greater than 400 nm. Furthermore, absorption spectra (Fig. 4) show that the absorbance is not negligible at wavelengths corresponding to the generated third harmonics nonlinearities (THG). It establishes that the absorption process impacts the THG response generated. As a result, in NLO calculations, the absorption coefficient α must be considered. Tab. 2 regroup the calculated values of absorption coefficients α for 532 nm (SHG) and 355 nm (THG).

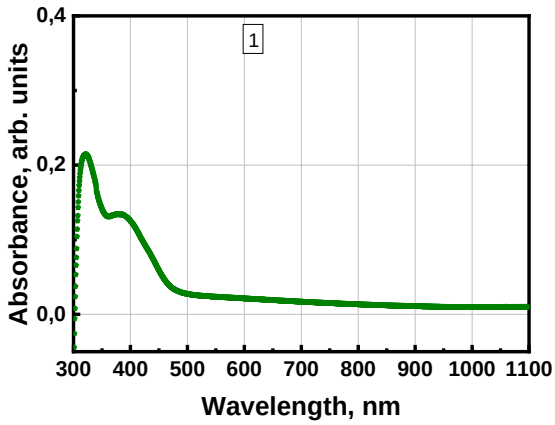

Figure 4: Absorption spectrum of the studied compound 1.

3.5.NLO Analysis:

-SHG results:

The anisotropic nonlinear optical conversion has a maximal SHG response at an incidence angle of 75°, which seems to dominate in P-polarization. We employed Y-cut quartz glass with a thickness of 1 mm as a reference material for SHG measurements. Tab 5. illustrate the estimated susceptibilities and shows that the SHG response for the studied compound 1 was stronger for the p-p input-output polarization setup than for the s-p approach. This discrepancy is related to the values of tensor components $\chi(2)$, which are responsible for the experiment's complementary scheme – $\chi(2)zzz$ and $\chi(2)zxx$. The theoretically expected ratio $\chi(2)zzz/\chi(2)zxx=3$ [53] for molecular systems. The structure of the studied compound is constituted of three aromatic rings, similar to compounds studied 2 with two substituents instead of one on the C13 carbon atom.

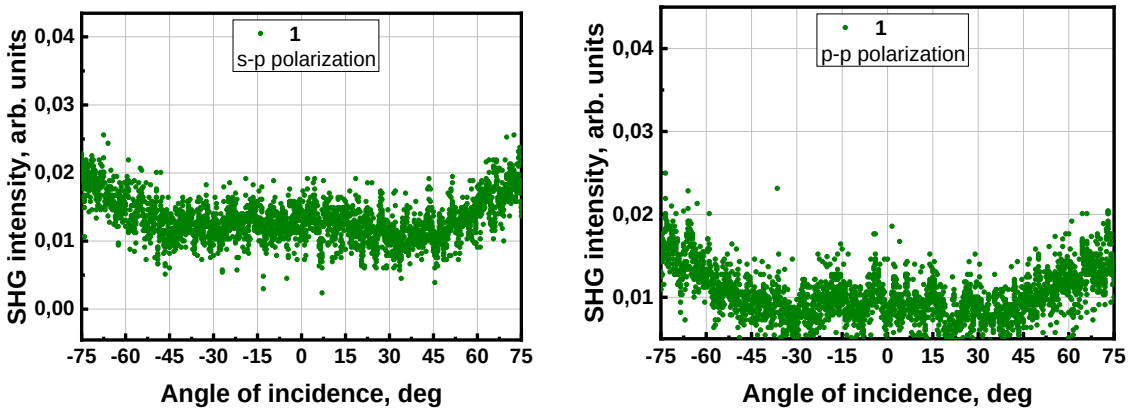

Figure 5: SHG response of 1 thin film in s- and p-polarization.

The quadratic susceptibility value for compound **1** is measured at a wavelength of 1064 nm on thin film, and it is estimated to be 0. 243 [pmV^{-1}] (Table 5). This value represents a quarter of the quartz susceptibility ($\chi^{(2)}$) value and is half of compound **2**. This result can be explained by the fact that the two methyl groups on the C13 carbon slow the electronic mobility and break the electronic conjunction of the phenyl ring.

Table 5: Second- and third-order nonlinear optical susceptibility.

Sample	$\chi^{(2)}$ [pmV^{-1}]		$\chi^{(3)}$ [10^{-22} m^2V^{-2}]
	s-p	p-p	p-p
Quartz	1.00		-
Silica	-		2.00
1	0.187	0.243	41.13
2	0.545	0.572	60.89

-THG results:

Figure 6 displays the third harmonic intensity of compound **1**. As a reference material for THG measurements, 1mm thick silica glass was employed. The susceptibilities ($\chi_{THG}^{<3>}$) were calculated using Formula 2. Table 5. shows the results. We might assume that the electronic contribution is included in the computed values using the third harmonic generation theory.

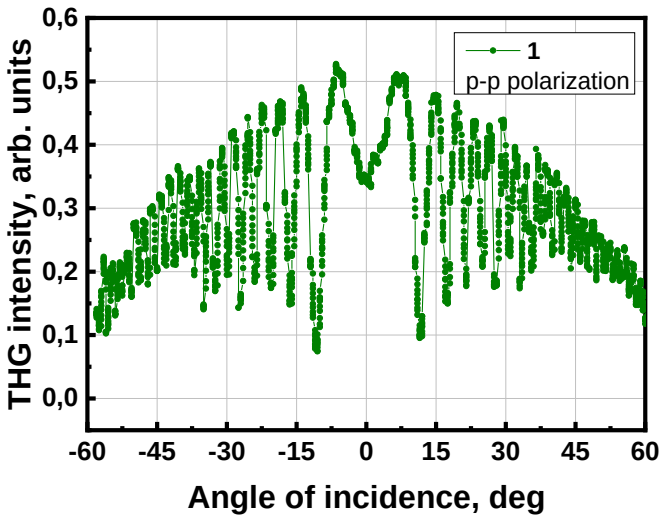

Figure 6: THG response of 1 thin film in p-polarization.

THG measurements for P-polarization were carried out on the studied thin film of 1, and their intensities as a function of incidence angle are shown in Fig. 6. By comparing the TH signal to that of silica glass, the THG susceptibility value for the studied compound is calculated and analyzed. The cubic susceptibility value of the 1 is measured at a wavelength of 1064 nm, and it is estimated to be 41.13 10^{-22} [m^2V^{-2}] (Table 5). This value is 20 times greater than silica's

susceptibility ($\chi_{THG}^{<3>}$) value and lower than compound 2. The steric hindrance may explain why compound 1 results are more significant than compound 2.

3.6. DFT Analysis:

3.6.1. UV-Vis spectral

Vertical excitation energies and oscillator strengths of title compounds were calculated using Time-dependent (TD-DFT) [54,55] to analyze the UV-spectra and determine the nature of the bonds' electronic transitions. The geometries of the electronic vertical excitation were optimized in the acetonitrile solvent with CAM-B3LYP/ 6-311G (d, p) basis set using the Polarizable Continuum Model (PCM). The results of a significant contribution of molecular orbitals to the formation of absorption bonds are listed in Table 6.

From compound **1**, it can be seen that the intense transitions localized at 280.77, 318.45 and 356.87 with assigned configurations H-2→L (81.41 %), H→L (78 %) and H→L+1 (64.56 %), respectively. In the case compound 2, the intense absorptions are shown at 245.44, 383.02, and 322.97, with the significant orbital contributions H-1→L+1 (85,46 %), H→L (81,52 %) and H→L+1 (69,25 %). According to Table 6, the major orbital of the two compounds studied shows the inverse relationship with oscillator strength. The highest is the compound which has a small oscillator strength. It can be observed in Fig. 7 that the theoretical absorption spectra reproduce well experimental spectrum. Hence, in the CAM-B3LYP hybrid, the excitation values were obtained in good agreement with that of experimental values.

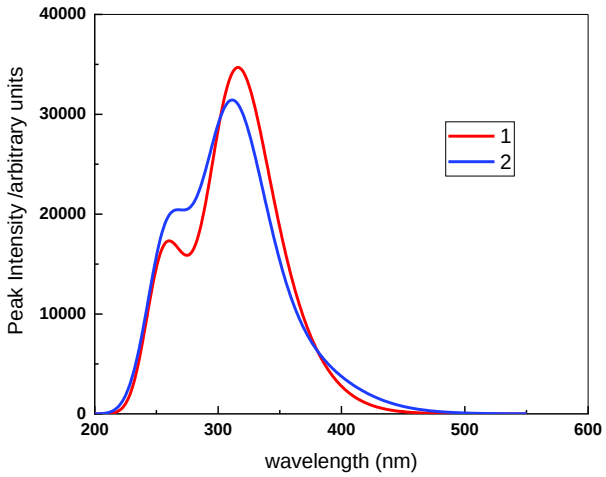

Figure 7. Simulation absorption spectra; red and blue lines represent the compounds 1 and 2 respectively, computed with Cam-B3LYP in acetonitrile solvent.

Table 6 Comparison among the experimental and calculated λ_{max} values, excitation energies E (eV) and oscillator strengths using TD-DFT/ CAM-B3LYP/6-31G(d,p).

Compounds	Absorption wavelength (λ_{cal} nm)	Excitation energy (eV)	Oscillator strength (f)	Transitions	(Major Contributions)
1	356.87	3.4742	0.1275	$H \rightarrow L$	(78 %)
	332.21	3.7321	0.0652	$H-5 \rightarrow L$	(39.82%)
	318.45	3.8934	0.4408	$H \rightarrow L+1$	(64.56 %)
	308.29	4.0217	0.3393	$H-1 \rightarrow L$	53.25 %
	280.77	4.4158	0.0248	H-2→L	(81,41%)
	265.99	4.6613	0.0952	H→L+2	(49,23%)
	262.85	4.7169	0.0273	H→L+7	(49,23%)
	260.98	4.7507	0.0326	H-3→L	(41,05%)
	256.97	4.8248	0.1572	H-1→L+1	(62,18 %)
	251.39	4.9319	0.1183	H- 4→L	(41,20 %)
2	383.02	3.2370	0.0770	H→L	81,52 %
	340.02	3.6464	0.1167	H-5→L	37,21 %
	322.97	3.8389	0.2046	H→L+1	69,25 %
	309.69	4.0035	0.5017	H-1→L	60,40 %
	277.54	4.4673	0.0655	H-2→L	55,28 %
	265.96	4.6617	0.1500	H→L+2	45,47 %
	265.47	4.6703	0.0834	H-3→L	31,91 %
	261.73	4.7372	0.0364	H→L+7	40,43 %
	261.57	4.7400	0.1207	H-4→L	42,29 %
	245.44	5.0515	0.0690	H-1→L+1	**85,46 %**

3.6.2. NLO response

The results of NLO properties for the title compound are summarized in Tables 7 and 8. The values obtained for compound 2 have been added for comparison. Moreover, the calculated values of the average polarizability (α), anisotropy of the polarizability ($\Delta\alpha$) and the first static hyperpolarizability (β_0) for **1** are equal to 49.963 Å^3, 1.26 × 10^{-30} esu, and 2.25 10^{-29} esu respectively. These values are 45.719 Å^3, 1.00 × 10^{-30} esu, and 1.21 10^{-29} esu respectively for compound **2**. By comparison, the first hyperpolarizability of **1** is almost two times (1.93) higher than that observed for compound **2** and is two orders of magnitude (225) larger than that of the standard NLO material Urea 0.13x10^{-30} esu [56,57]. The second-order hyperpolarizability for compound **1** is **1.44x10^{-27}** esu and is slightly higher than for compound 2 (1.21x10^{-27} esu). This can be explained by the fact that the CH3 groups in compound **1** act as a donor groups, which may enhance the first hyperpolarizability when compared to compound **2**. These results indicate that compound **1** is a promising candidate for use as nonlinear optical material than **2**. It is expected that

Table 7. Calculated all β and $\langle\gamma\rangle(0;0,0,0)$ components and β_{tot}, using B3LYP/6-31+G (p, d) for the both molecules **1** and 2.

Components	**1**	**2**
$\beta_{xx\,x}$	-2120,37	-864,91
β_{xxy}	-1,59	54,82
β_{xyy}	-347,24	148,50
β_{yyy}	-53,83	309,70
β_{xxz}	319,49	156,30
β_{xyz}	149,40	-80,94
β_{yyz}	-44,40	-61,42
β_{xzz}	-45,00	-0,880747
β_{yzz}	-109,32	-55,85
β_{zzz}	405,81	462,80
β_{tot} (esu)	$2{,}25\times10^{-29}$	$1{,}16\times10^{-29}$
γ_{xxxx}	448200,00	328670,00
γ_{yyyy}	98707,10	83312,00
γ_{zzzz}	50037,60	44616,10
γ_{xxyy}	65198,50	58667,90
γ_{xxzz}	33544,00	38647,60
γ_{yyzz}	19314,30	25517,30
$\langle\gamma\rangle$(esu)	$1{,}44\times10^{-27}$	$1{,}21\times10^{-27}$

Table 8. Calculated total dipole moment μ (Debye), polarizability $\alpha(\text{Å}^3)$, anisotropy of the polarizability (esu) and the first hyperpolarizability β_0 (esu) for compounds 1 and 2.

Components	1	2
μ_x	-1.1342	-1.7794
μ_y	-3.1504	-2.7035
μ_z	6.5370	7.7212
μ_{tot} (Debye)	7.3447	8.3721
α_x	428.378	384.855
α_y	321.237	282.908
α_z	261.907	257.826
$\alpha(\text{Å}^3)$	49,963	45,719
$\Delta\alpha$ (esu)	1.26×10^{-30}	1.00×10^{-30}

As shown in Table 9, the reactivity parameters displayed that compound **1** has a high value of ionization potential (6.006 eV). In addition, a high value of hardness (1.637 eV)**,** low values of

softness (0.610 eV) and a high energy gap (3.274 eV) means that the **1** has high kinetic stability (lower chemical reactivity) [58].

Table 9. Quantum chemical parameters of the 1 and 2 calculated at DFT level using the B3LYP/ 6-311G (d, p) basis set.

Reactivity Parameters (Units in eV)	**Compounds**	
	1	2
Total energy (Hartree)	**-32755,474**	-30615,311
E_{HOMO}	-6.020	-5.942
E_{LUMO}	-5,942	-2,8973208
ΔE	3.274	**3.045**
E_{HOMO-1}	-6,653	-6,902
E_{LUMO+1}	-2,327	-2,257
ΔE (E_{HOMO-1} E_{LUMO+1})	4,325	4,645
I	**6,006**	**5,942**
A	2,745	2,897
X	4,382	4,420
H	**1,637**	**1,522**
Σ	0,610	0,656
μ	-4,382	-4,420
W	15,726	14,875
Back-d	-0,409	-0,380

3.6.3. Frontier molecular orbitals (HOMO - LUMO) analysis

The frontier molecular orbitals analysis is essential in fundamental chemistry to reveal the chemical reactivity of the compounds. Therefore, the optimized structures of both compounds in the gas phase were calculated using the density functional theory (DFT) at B3LYP/6-311G (d, p) basis set to study the NLO properties.

Table 9 shows the total energy, E_{LUMO}, E_{HOMO} and ΔE_{L-H} energy gap; according to the E_{total} value, the **1** presented high stability. In addition, in this work, the energy gap value of compound **1** is **(**3.274 eV) high than that of the compound 2 (3.045 eV)**,** an opposite correlation between

the energy gap and the hyper polarizabilities [59]. In general, the band gap values reveal that the two molecules have high chemical reactivity. The high value of E_{HOMO} represents the ability of the compound to donate electrons, while the lowest E_{LUMO} indicates the ability to accept electrons. Therefore, the 3D plots of the frontier molecular orbitals HOMO and LUMO, for both compounds are shown in Fig. 8. It can be seen from (Fig.8) that the two compounds (**1** and 2) have a similar HOMO electron density distribution with a particular focus on the C8H4-N3 groups.

3.6.4. Molecular electrostatic potential surface (MEP)

The molecular electrostatic potential was used as a helpful method for indicating the chemical reactivity sites of compounds shown in Fig. 8. Different colors show the electron density isosurface at different points. The red color shows regions of most negative electrostatic potential, electrophilic active region. The blue represents regions of the most positive electrostatic potential, nucleophilic active region, and the green illustrates a region of zero potential; the potential rises in the following order red < orange < yellow < green < blue [60,61]. The electron-rich regions are mainly localized around heteroatoms and conjugated double bonds. The oxygen, nitrogen, and CN groups indicate negative regions that favor the electrophilic attacks. On the other hand, hydrogen atoms have a positive sign (blue color) that favors nucleophilic attacks.

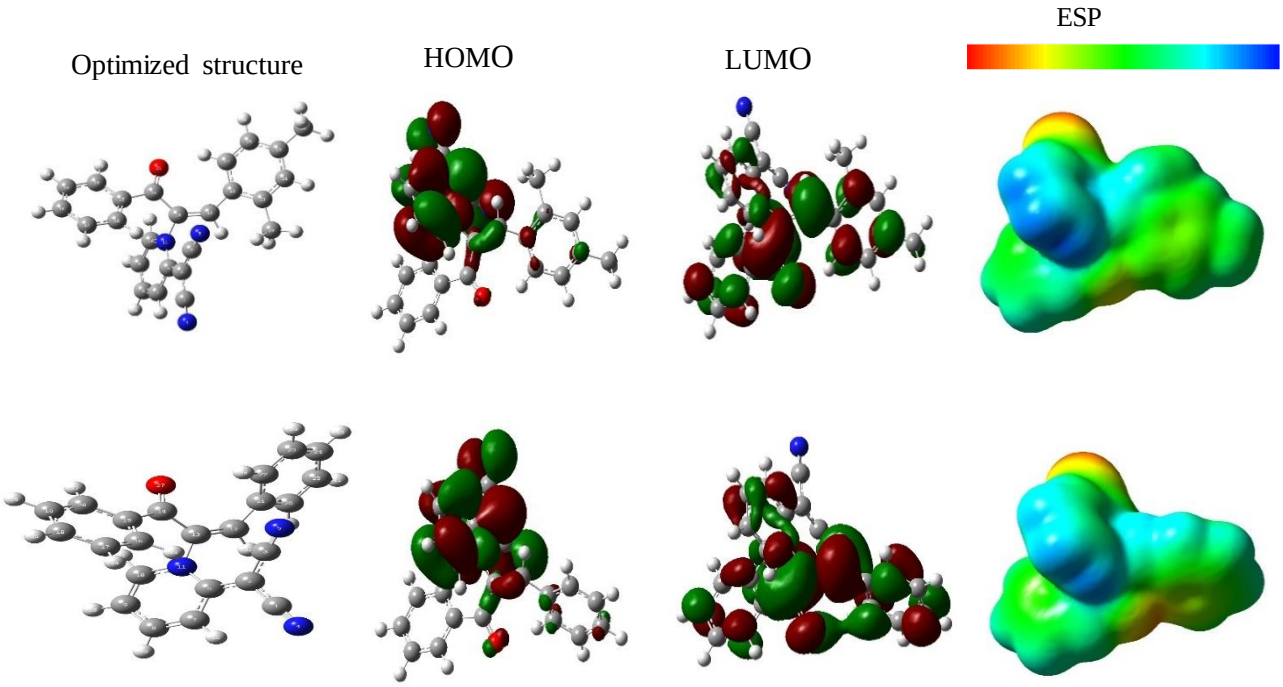

Figure 8. Frontier molecular orbitals HOMO and LUMO density distribution in the gas phase and electrostatic potentials mapped on the electron density (isovalue = 0.0004 a.u) for title compound calculated at B3LYP/6-311G (d, p) level.

Conclusion

In conclusion, this paper discusses the synthesis, structural characterization, and nonlinear optical (NLO) characteristics of a chalcone derivative: (Z)-2-(1-(1-(2,4-dimethylphenyl)-3-oxo-3-phenylprop-1-en-2-yl)pyridin-2(1*H*)ylidene) malononitrile. According to single crystal analysis, the structural geometry of 1 assumes a Z conformation and can be characterized in centrosymmetric space groups. Weak C-H...N, and C-H...O hydrogen bonds, as well as C—H...p interactions, stabilize the crystal structures of the studied compound. Second and third harmonic generation (SHG and THG) measurements at 1064 nm were used to analyze quadratic and cubic NLO susceptibilities on thin films. We have used the corona poling approach to invert the symmetry for the induced second harmonic generation measurements. To entirely comprehend the second and third-order NLO phenomena, the detailed DFT quantum calculations have also been effectuated to acquire the dispersion-free dipole polarizabilities, second and third-order hyperpolarizabilities and susceptibilities for 1-2. We found that the quadratic and the cubic nonlinear responses decrease proportionally with the nature and the number of electron-donating substituent groups on the conjugated system. The combined findings demonstrate that the NLO properties depend only on the steric hindrance and the chemical structure, that is, the system of π-conjugated electrons. The experimental nonlinearity analyses for the examined compounds, as reflected by their susceptibility to second and third-order NLO characteristics, are in good accord with the quantum results.

Acknowledgements

We are grateful for the measurement time on the X-ray diffraction platform PMD²X of the Institute Jean Barriol, Université de Lorraine.

References

[1] Ralph, T. C.; Boyd, R. W. Better Computing with Photons. Science 2007, 318, 1251-1252.
[2] H.S. Nalwa, S. Miyata, Nonlinear Optics of Organic Molecules and Polymers, CRC press, 1996.
[3] Kajzar, F.; Swalen, J. D. Eds., Organic Thin Films for Waveguiding Nonlinear Optics; Gordon and Breach, Amsterdam, 1996.
[4] R.W. Boyd, Nonlinear Optics, Academic Press, 2003.
[5] Andraud, C., Maury, O. (2009). Lanthanide complexes for nonlinear optics: from fundamental aspects to applications. European Journal of Inorganic Chemistry, 2009(29-30), 4357-4371.
[6] M. Maaza, N. Mongwaketsi, M. Genene, G. Hailu, G. Garab, B. Sahraoui and D. Hamidi, J. Porphyrins Phthalocyanines, 2012, 16, 985–995.
[7] I. Fuks-Janczarek, J. Luc, B. Sahraoui, F. Dumur, P. Hudhomme, J. Berdowski and I. V. Kityk, J. Phys. Chem. B, 2005, 109, 10179–10183.
[8] D'silva, E. D., Podagatlapalli, G. K., Rao, S. V., Rao, D. N. & Dharmaprakash, S. M. (2011). Cryst. Growth Des. 11, 5326–5369.

[9] Y. Xiong, X.H. Zou, J.Z. Wu, H.Y. Yang, L.N. Ji, Synth. React. Inorg. Met.-Org. Chem., 1998, pp. 1445–1454.
[10] T. Cardinaels, J. Ramaekers, P. Nockemann, K. Driesen, K.V. Hecke, L.V. Meervelt, S. Lei, S.D. Feyter, D. Guillon, B. Donnio, K. Binnemans, Imidazo[4,5-f]-1,10-phenanthrolines: versatile ligands for the design of metallomesogens, Chem. Mater. 20 (2008) 1278–1291.
[11] J. Wang, S. Xu, F. Zhao, H. Xia, Y. Wang, Computational and spectroscopic studies of the imidazole-fused phenanthroline derivatives containing phenyl, naphthyl, and anthryl groups, J. Mol. Struct. 1108 (2016) 46–53.
[12] J.Z. Wu, L. Li, T.X. Zeng, L.N. Ji, Effect of pyridine on the expression of cytochrome P450 isozymes in primary rat hepatocyte culture, Mol. Cell. Biochem. 173 (1997) 103–111.
[13] A. Airinei, R. Tigoianu, R. Danac, C.M. Al Matarneh, D.L. Isac, Steady state and time resolved fluorescence studies of new indolizine derivatives with phenanthroline skeleton, J. Lumin. 199 (2018) 2–12.
[14] C. Sall, A.-D. Yapi, N. Desbois, S. Chevalley, J.-M. Chezal, K. Tan, J.-C. Teulade, A. Valentin, Y. Blache, Design, synthesis, and biological activities of conformationally restricted analogs of primaquine with a 1,10-phenanthroline framework, Bioorg. Med. Chem. Lett. 18 (2008) 4666–4669.
[15] M.C. Nielsen, A.F. Larsen, F.H. Abdikadir, T. Ulven, Phenanthroline-2,9-bistriazoles as selective G-quadruplex ligands, Eur. J. Med. Chem. 72 (2014) 119–126.
[16] (a) S. Thomas, G. Ruiz, G. Ferraudi, Preparation and reactivityof pendent CO2RhIII(phthalocyanine) bound to a poly(acrylate) backbone. Effects of the hypercoiled backbone on the association, photochemical, and thermal redox reactions of the pendent macrocycle, Macromolecules 39 (19) (2006) 6615–6621.
[17] T. Maldona-do, G. Ferraudi, G. Lappin, F. Godoy, Kinetic and mechanistic observations on the photoinduced isomerization reaction of organo-metallic chalcones: a steady state and flash photolysis study, ChemPhotoChem 2 (2) (2018) 95–104.
[18] J. Jayabharathi, V. Thanikachalam, M. Venkatesh, PerumalPhotophysical studies of fused phenanthrimidazole derivatives as versatile π-conjugated systems for potential NLO applications, Spectrochim. Acta A Mol. Biomol. Spectrosc. 92 (2012) 113–121.
[19] C.R. Moylan, R.D. Miller, R.J. Twieg, K.M. Betterton, V.Y. Lee, T.J. Matray, C. Nguyen, Synthesis and nonlinear optical properties of donor-acceptor substituted triaryl azole derivatives, Chem. Mater. 5 (1993) 1499–1508.
[20] G.S. Hong, Y.P. Zou, A.L. Antaris, S. Diao, D. Wu, K. Cheng, X.D. Zhang, C.X. Chen, B. Liu, Y.H. He, J.Z. Wu, J. Yuan, B. Zhang, Z.M. Tao, C. Fukunaga, H.J. Dai, Ultrafast fluorescence imaging in vivo with conjugated polymer fluorophores in the second near-infrared window, Nat. Commun. 5 (2014) 4206.
[21] A. Bencini, V. Lippolis, 1,10-Phenanthroline: a versatile building block for the construction ofligands for various purposes, Coord. Chem. Rev. 254 (17) (2010) 2096–2180
[22] K. Bouchouit, Z. Essaidi, S. Abed, A. Migalska-Zalas, B. Derkowska, N. Benalicherif, M. Mihaly, A. Meghea, B. Sahraoui, Chem. Phys. Lett. 455 (2008) 270
[23] S. Arroudj, M. Bouchouit, K. Bouchouit, A. Bouraiou, L. Messaadia, B. Kulyk, V. Figa, S. Bouacida, Z. Sofani, S. Taboukhat, Opt. Mater. 56, 116 (2016)
[24] M. Bouchouit, Y. Elkouari, L. Messaadia, A. Bouraiou, S. Arroudj, S. Bouacida, S. Taboukhat, K. Bouchouit, Opt. Quant. Electron. 48 (2016) 178.
[25] K. Bouchouit, E. Bendeif, H. E. Ouazzani, S. Dahaoui, C. Lecomte,N. Benali-cherif, B. Sahraoui, Correlation between structural studiesand third order nlo properties of selected new quinolinium semi-organic compounds, Chem. Phys. 375 (2010) pp 1 – 7.

[26] J. Luc, K. Bouchouit, R. Czaplicki, J.-L. Fillaut, B. Sahraoui, Study of surface relief gratings on azo organometallic films in picosecond regime. Opt. Express **16**, 15633–15639 (2008)
[27] F.A. Sahki, A. Bouraiou, S. Taboukhat, L. Messaadia, S. Bouacida, V. Figa, K. Bouchouit, B. Sahraoui, Design and synthesis of highly conjugated electronic phenanthrolines derivatives for remarkable NLO properties and DFT analysis. Optik **241**, 166949 (2021).
[28] H. Belahlou, K. Waszkowska, A. Bouraiou, E. Bendeif, S. Taboukhat, K. Bouchouit, B. Sahraoui, New architecture of organo electronic chalcones derivatives: synthesis, crystal structures and optical properties. Opt. Mater. **108**, 110188 (2020).
[29] K. Bouchouit, H. Bougharraf, B. Derkowska-Zielinska, N. Benalicherif, B. Sahraoui, Reversible phase transition in semi-organic compound p-nitroanilinium sulfate detected using second harmonic generation as a tool. Opt Mater **48**, 215–221 (2015).
[30] Sheldrick, G.M. Acta Cryst. 2015, C71, 3–8.
[31] Farrugia, L. J. J. Appl. Cryst. 1999, 32, 837–838.
[32] B. Sahraoui, J. Luc, et al. J. Opt. A, Pure Appl. Opt. 11, 2009.
[33] A. Zawadzka, K. Waszkowska, et al. Dyes and Pigments, Volume 157, Pages 151-162, 2018.
[34] G. J. Lee, et. al. J. Kor. Phys. Soc., 39(5), 912-915, 2001.
[35] S.K. Kurtz, J. Jerphagnon, M.M. Choy, Landolt-Boernstein New Ser. 11 (1979) 671.
[36] K. Kubodera, H. Kobayashi, Mol. Crys. Liq. Crys. Inc. NLO, 182:1, 103-113, 1990.
[37] F. Kajzar, Y. Okada-Shudo, C. Merrit, Z. Kafafi, Synth. Met. 117, 2001.
[38] Sahraoui, B.; Luc, J.; Meghea, A.; Czaplicki, R.; Fillaut, J.L.; Migalska-Zalas, A. Nonlinear optics and surface relief gratings in alkynyl–ruthenium complexes. Journal of Optics A: Pure and Applied Optics 2009, 11 (2), 024005.
[39] M.J. Frisch, G.W. Trucks, H.B. Schlegel, G.E. Scuseria, M.A. Robb, J.R. Cheeseman, G. Scalmani, V. Barone, B. Mennucci, G.A. Petersson, H. Nakatsuji, M. Caricato, X. Li, H.P. Hratchian, A.F. Izmaylov, J. Bloino, G. Zheng, J.L. Sonnenberg, M. Hada, M. Ehara, K. Toyota, R. Fukuda, J. Hasegawa, M. Ishida, T. Nakajima, Y. Honda, O. Kitao, H. Nakai, T. Vreven, J.A. Montgomery Jr., J.E. Peralta, F. Ogliaro, M. Bearpark, J.J. Heyd, E. Brothers, K.N. Kudin, V. N. Staroverov, T. Keith, R. Kobayashi, J. Normand, K. Raghavachari, A. Rendell, J.C. Burant, S.S. Iyengar, J. Tomas i, M. Cossi, N. Rega, J.M. Millam, M. Klene, J.E. Knox, J.B. Crossi, V. Bakken, C. Adamo, J. Jaramillo, R. Gomperts, R.E. Stratmann, O. Yazyev, A.J. Austin, R. Cammi, C. Pomelli, J.W. Ochterski, R. L. Martin, K. Morokuma, V.G. Zakrzewski, G.A. Voth, P. Salvador, J.J. Dannenberg, S. Dapprich, A.D. Daniels, O. Farkas, J.B. Foresman, J.V. Ortiz, J. Cioslowski, D.J. Fox, Gaussian 09, Revision C.01, Gaussian Inc., Wallingford CT, 2009.
[40] R. Dennington, T. Keith, J. Millam, GaussView Version 5.0.9, Semichem Inc. Shawnee Mission KS, 2009.
[41] A.D. Becke, Density-functional thermochemistry. III. The role of exact exchange, J. Chem. Phys. 98 (1993) 5648–5652.
[42] C. Lee, W. Yang, R.G. Parr, Development of the Colle-Salvetti correlation-energy formula into a functional of the electron density, Phys. Rev. B 37 (1988) 785–789.
[43] X.H. Wang, D.P. West, N.B. McKeown, T.A. King. J. Opt. Soc. Am. B, 15 (1998) 1895-1903.
[44] Z.C. Koopmans, T. Uber die Zuordnung von Wellenfunktionen und Eigenwerten zuden einzelnen Elektronen eines Atoms, Physica 1 (1934) 104–113.
[45] Demircioğlu, Z., Kaştaş, G., Kaştaş, Ç. A., & Frank, R. (2019). Spectroscopic, XRD, Hirshfeld surface and DFT approach (chemical activity, ECT, NBO, FFA, NLO, MEP, NPA& MPA) of (E)-4-bromo-2-[(4-bromophenylimino) methyl]-6-ethoxyphenol. Journal of Molecular Structure, 1191, 129-137.

[46] Kumar, R., Karthick, T., Parol, V., Rawat, P., Tandon, P., Gupta, A., ... & Upadhyaya, V. Spectroscopic characterization and structural insights of 4-[(1E)-3-(4-methoxyphenyl)-3-oxoprop-1-en-1-yl] phenyl 4-methylbenzene-1-sulfonate using vibrational, electronic spectra and quantum chemical calculations. Journal of Molecular Structure, 1225, 129144.
[47] Gültekin, Z., Demircioğlu, Z., Frey, W., & Büyükgüngör, O. (2020). A combined experimental (XRD, FT-IR, UV-VIS and NMR) and theoretical (NBO, NLO, local & global chemical activity) studies of methyl 2-((3R, 4R)-3-(naphthalen-1-yl)-4-(phenylsulfonyl) isoxazolidin-2-yl) acetate. Journal of Molecular Structure, 1199, 126970.
[48] S. K. Wolff, D. J. Grimwood, J. J. McKinnon, M. J. Turner, D. Jayatilaka, M. A. Spackman, Crystal Explorer 3.1, University of Western Australia, 2013.
[49] C. Jelsch, K. Ejsmont, L. Huder, IUCr J. 1 (2014) 119-128. https://doi.org/10.1107/S2052252514003327.
[50] Spackman, M.A.; Jayatilaka, D. Hirshfeld Surface Analysis. CrystEngComm 2009, 11, 19–32.
[51] Madni, M.; Ahmed, M.N.; Hafeez, M.; Ashfaq, M.; Tahir, M.N.; Gil, D.M.; Galmés, B.; Hameed, S.; Frontera, A. Recurrent π–π Stacking Motifs in Three New 4,5-Dihydropyrazolyl–Thiazole–Coumarin Hybrids: X-ray Characterization, Hirshfeld Surface Analysis and DFT Calculations. New J. Chem. 2020, 44, 14592–14603.
[52] J. J. McKinnon, D. Jayatilaka, M. A. Spackman, Chem. Commun. 37 (2007) 3814-3816. https://doi.org/10.1039/b704980c.
[53] P.N. Prasad, D.J. Williams, Introduction to Nonlinear Optical Effects in Molecules & Polymers, Wiley, New York (1991)
[54] G. Scalmani, M. J. Frisch, B. Mennucci, J. Tomasi, R. Cammi, V. Barone, "Geometries and properties of excited states in the gas phase and in solution: Theory and application of a timedependent density functional theory polarizable continuum model", J. Chem. Phys., 2006, 124, 094107.
[55] J. Tomasi, B. Mennucci and R. Cammi, Chem. Rev., 2005, 105, 2999–3094.
[56] Alyar, H., Kantarci, Z., Bahat, M., & Kasap, E. (2007). Investigation of torsional barriers and nonlinear optical (NLO) properties of phenyltriazines. Journal of molecular structure, 834, 516-520.
[57] Adant, C., Dupuis, M., & Bredas, J. L. (1995). Ab initio study of the nonlinear optical properties of urea: electron correlation and dispersion effects. International Journal of Quantum Chemistry, 56(S29), 497-507.
[58] Demircioğlu, Z., Kaştaş, G., Kaştaş, Ç. A., & Frank, R. (2019). Spectroscopic, XRD, Hirshfeld surface and DFT approach (chemical activity, ECT, NBO, FFA, NLO, MEP, NPA& MPA) of (E)-4-bromo-2-[(4-bromophenylimino) methyl]-6-ethoxyphenol. Journal of Molecular Structure, 1191, 129-137.
[59] Liyanage P.S., De Silva R.M., De Silva K.M.N., Nonlinear optical (NLO) properties of novel organometallic complexes: high accuracy density functional theory (DFT) calculations, J. Mol. Struct. (Theochem), 2003, 639, 195-201. DOI: 10.1016/j. theochem.2003.08.009.
[60] J.S. Murray, P. Politzer, The electrostatic potential: an overview, Wiley Interdiscip. Rev. Comput. Mol. Sci. 1 (2011) 153–163.
[61] P. Sjoberg, P. Politzer, Use of the electrostatic potential at the molecular surface to interpret and predict nucleophilic processes, J. Phys. Chem. 94 (1990) 3959–3961